

Novel bounds on decaying axionlike particle dark matter from the cosmic background

Sara Porras-Bedmar¹ ^{*}, Manuel Meyer² , and Dieter Horns¹ 

¹*Universität Hamburg, Luruper Chaussee 149, D-22761 Hamburg, Germany*

²*CP3-Origins, University of Southern Denmark, Campusvej 55, DK-5230 Odense M, Denmark*

(Dated: October 31, 2024)

The cosmic background (CB) is defined as the isotropic diffuse radiation field with extragalactic origin found across the electromagnetic spectrum. Different astrophysical sources dominate the CB emission at different energies, such as stars in the optical or active galactic nuclei in x rays. Assuming that dark matter consists of axions or axionlike particles with masses on the order of electron volts or higher, we expect an additional contribution to the CB due to their decay into two photons. Here, we model the CB between the optical and x ray regimes, and include the contribution of decaying axions. Through a comparison with the most recent direct and indirect CB measurements, we constrain the axion parameter space between masses $0.5\text{eV} - 10^7\text{eV}$ and improve previous limits on axion-photon coupling derived from the CB by roughly an order of magnitude, also reaching the QCD band. We further study the contribution of axions decaying in the Milky Way halo and characterize the axion parameters that would explain the tentative excess CB emission observed with the Long Range Reconnaissance Imager instrument on-board the New Horizons probe.

Keywords: Cosmic background radiation; Cold dark matter; Axions

I. INTRODUCTION

The Λ CDM cosmology relies on the existence of non-baryonic cold dark matter (DM), which makes up around 85% of the matter content in the Universe [1]. So far, evidence for dark matter comes solely from its gravitational interaction revealing itself in astrophysical observations on different scales [2]. One possibility is that dark matter is made up from so-far undetected fundamental particles. Axions are one such candidate [3, 4].

The axion is a proposed pseudo-Nambu-Goldstone boson that arises from the Peccei-Quinn solution to the strong CP problem in QCD, thus explaining the nonobservation of the electric dipole moment of the neutron [5, 6]. Axions are predicted to couple to photons, with their coupling being proportional to the axion mass [7]. Axionlike particles (ALPs) are an extension of axions that do not solve the strong CP problem and whose mass and coupling are independent parameters. Just like axions, ALPs are a well-motivated candidate to explain DM [8].

The search for axions and ALPs has significantly intensified over recent years: direct searches are carried out with haloscopes [9–12] and helioscopes [13–17], axion and ALP production is tested in laboratories [18–23], and in astrophysical environments [24–29], sometimes assuming ALPs are DM [30–36]. Many of these searches make use of the coupling of ALPs to photons, $\mathcal{L}_{a\gamma} = -\frac{1}{4}g_{a\gamma}F_{\mu\nu}\tilde{F}_{\mu\nu}a$, with photon coupling $g_{a\gamma}$, the ALP field strength a , and $F_{\mu\nu}$ the electromagnetic field tensor (and its dual $\tilde{F}_{\mu\nu}$). This coupling can lead to photon-ALP conversion in magnetic fields or ALP decay into two photons. We focus on an indirect astrophysical

method assuming ALPs as DM that could contribute to the cosmic background (CB).

The CB is defined as the homogeneous and isotropic diffuse radiation field with extragalactic origin. It covers the entire electromagnetic spectrum, from radio waves to γ rays, so different detection techniques and observations are necessary to trace it. Recent reviews and data compilations of CB measurements are available from Refs. [37, 38]. Various astrophysical processes contribute to the CB at different wavelengths. The potential decay of ALPs into two photons would add to the CB intensity, its exact spectral shape given by the ALP mass and photon coupling strength, and its energy shifted by cosmological expansion. Limits over a broad range of mass and coupling constants were derived in Ref. [30].

The cosmic optical background (COB) has a special importance regarding ALP searches. Given the relation between axion mass and decay wavelength, the decay from the QCD axion would contribute in this regime. The New Horizons probe (NH) has been traveling through the outskirts of the Solar System, and has taken various measurements of the optical CB through the years, some of them over 51 A.U. away from Earth [39, 40]. These measurements are relevant because the zodiacal light [41], solar light scattered by dust, is less prevalent in the outer region of the Solar System. Zodiacal light is a bright foreground in the optical and infrared bands, and its modeling currently is not sufficiently accurate to subtract it reliably from the measurements to obtain the comparably weak COB. This makes the NH measurements unique, since it is the only occasion where we have subdominant interplanetary dust contamination in an optical observation.

After the extraction of the residual foreground emission, the authors of Ref. [40] found a $> 5\sigma$ mismatch in intensity between the NH measurement and the galaxy counts calculated by previous works. Galaxy counts are defined as the minimum amount of intensity that galax-

* sara.porras.bedmar@uni-hamburg.de

ies would contribute to the COB [42, 43], and they can be understood as COB lower limits. This excess has been interpreted in terms of axion decay [44, 45]. However, no other COB measurements were included in their study. Any axion or ALP interpretation must also be consistent with constraints on the COB at other optical wavelengths. Furthermore, a recent analysis of a larger dataset obtained with Long Range Reconnaissance Imager (LORRI) suggests a much reduced excess compatible at the 1.4σ level with Galaxy number counts [46].

Other spectral regimes are also interesting to study. In this work we focus on the broad wavelength range between 10^{-6} and $10\mu\text{m}$ or from x rays to optical wavelengths. The three regimes included here are the cosmic x-ray, ultraviolet and optical backgrounds (CXB, CUB and COB, respectively). Longer wavelengths would mean entering the infrared regime or CIB. The infrared part of the CB requires additional assumptions about the dust population [47, 48], which we leave for future study. Smaller wavelengths mean studying the γ -ray background (CGB). This would entail modeling the different populations of active Galactic nuclei (AGN) and accounting for the absorption of γ rays in the intergalactic medium. We also leave this for future work.

In summary, the goals of our study can be summarized as follows:

1. Investigate the interpretation of the NH measurement through axion decay in light of the excess reported in Ref. [40] and the updated result in Ref [46]. For this we develop our own model of the COB.
2. Derive novel constraints on DM axions and ALPs through their contribution to the CB from optical to x rays taking astrophysical emission into account.
3. Investigate the decay contribution from the local Milky Way DM halo. A high DM local density entails an extra contribution to CB measurements.

Throughout this work, we use ΛCDM cosmology with $\Omega_\Lambda = 0.7$, $\Omega_m = 0.3$ and $\Omega_{\text{baryons}} = 0.045$ (as the fraction of matter made up from baryons) [1]. We take a value for the Hubble constant of $H_0 = 70\text{ km s}^{-1}\text{ Mpc}^{-1}$, in order to be consistent with previous analyses whose results are used here.

The paper is structured as follows: in Sec. II we describe the observational data that we are going to work with. Then, in Sec. III we describe the theoretical background of astrophysical processes that form the CB and its modeling. In addition to the CB, we mainly include the axion/ALP decay, the DM host halo, and stellar populations. In Sec. V we present our results from modeling and the constraints to axions. The results are discussed in Sec. VI and we conclude in Sec. VII.

II. MEASUREMENTS OF THE CB

The CB has been measured across the electromagnetic spectrum using various instruments on different satellites. We use the data compilations provided by Refs. [37, 38], which are shown in Fig. 1.

A. COB

Following Ref. [38], we consider three different types of COB measurements: lower and upper limits, as well as tentative measurements.

Upper limits have been calculated by taking the background flux from optical photometric images [43, 50–52] and subtracting resolved foreground sources such as stars and galaxies, but also diffuse galactic emission. We treat these values as upper limits, since there might be unaccounted contributions to the images, or the zodiacal light could be wrongly subtracted. These measurements are shown in Fig. 1 as open markers.

Lower limits are calculated from galaxy counts [42, 43]. This is done by counting the number and luminosity of galaxies in optical photometric images. Galaxy counts provide the minimum amount of intensity that galaxies would contribute to the CB. Therefore, these measurements can be regarded as lower limits, since any truly diffuse component is not included. They are represented with filled data points in Fig. 1.

The NH data points are shown as stars in Fig. 1. There is a clear mismatch between the value reported in Ref. [40] and the rest of the lower limits, which is however much less severe with the latest value reported in Ref. [46]. We will study their implications using them either as an upper limit and a measurement of the CB.

B. CUB and CXB

The CUB intensity is attenuated because of photoionization in the neutral gas of the interstellar medium. Therefore, fewer measurements are generally available in this wavelength regime. The measurements and upper limits of the CUB we use here have been compiled from spectroscopic surveys. The values shown are the background noise that remains after subtracting all foregrounds from the spectra. Some data were given with a certain confidence interval, defining the background as a value with uncertainties, which we represent in Fig. 1 as empty symbols with error bars. Other values are provided as hard upper limits, which are represented with empty symbols with a downward-pointing arrow.

The CXB measurements are derived from x ray surveys by using the background of images after subtraction of individual sources [53], or using the Earth occultation technique [54, 55]. They are depicted as filled symbols in Fig. 1.

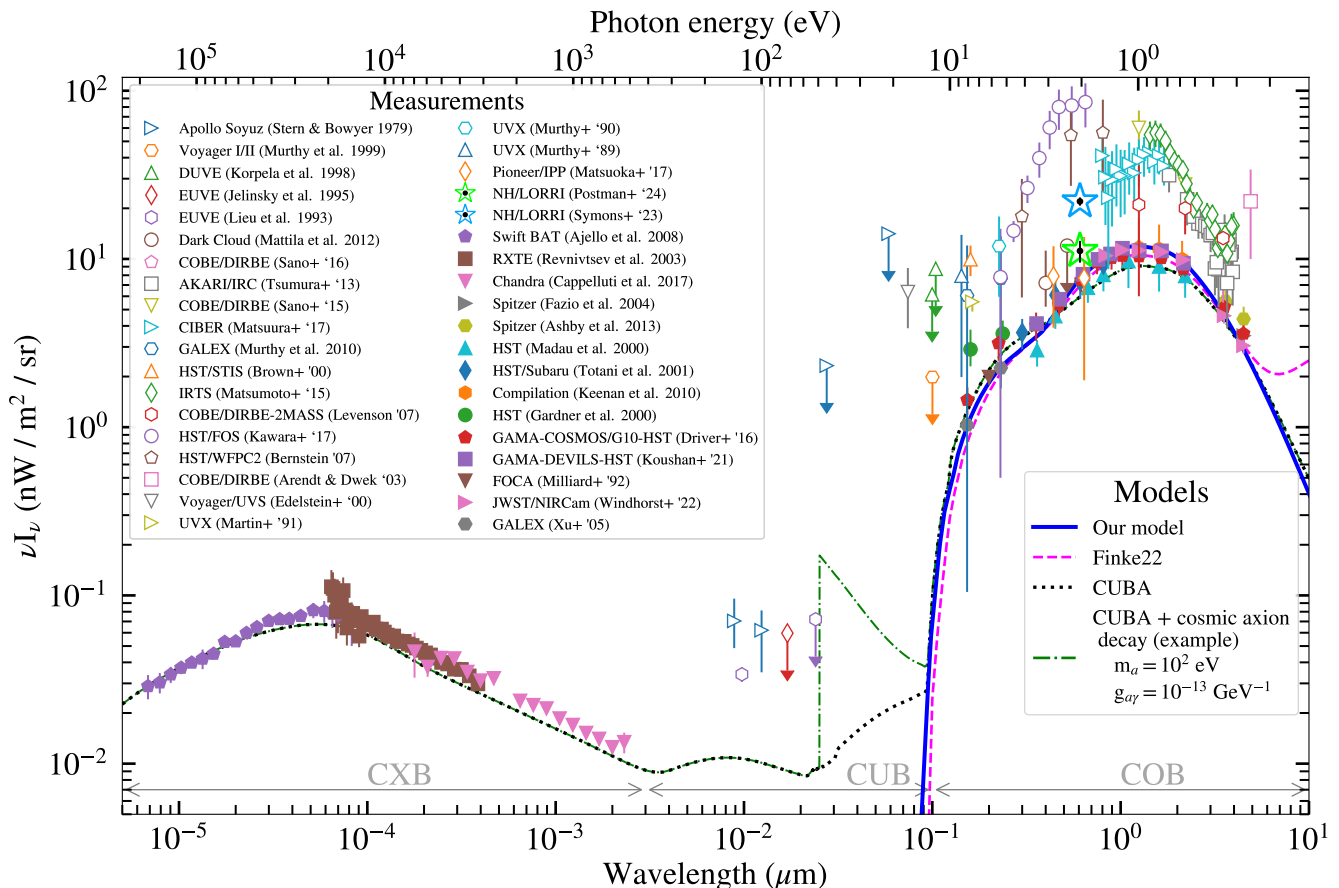


FIG. 1: Overview of the CB measurements used here. Data taken from compilations provided by Refs. [37, 38], in the wavelength range $3 \times 10^{-6} - 5 \mu\text{m}$. We show upper limits (open symbols), lower limits or measurements (filled symbols), and measurements (green and blue star). More details about the different kinds of measurements are given in Sec. II. Also displayed are the models used here: our model (explained in Sec. III B 1), the model developed by Finke *et al.* [48] and the CUBA model [49].

III. MODELING THE CB

When a source population produces emission, its contribution to the CB intensity can be calculated as [56]

$$\nu I_\nu(\lambda, z) = \frac{c^2}{4\pi\lambda} \int_z^{z_{\max}} \varepsilon_{\nu'} \left(\lambda \frac{1+z}{1+z'}, z' \right) \left| \frac{dt}{dz'} \right| dz', \quad (1)$$

with

$$\frac{dt}{dz} = \frac{-1}{(1+z)H(z)}, \quad (2)$$

where we integrate the emissivity $\varepsilon_\nu(\lambda, z)$ of the source population over the time it has been emitting. The emissivity depends on wavelength, which is redshifted over cosmic times, and the redshift itself. The maximum redshift z_{\max} defines the redshift at which the population started emitting. The Hubble parameter is defined by the Λ CDM parameters as $H(z) = H_0 \sqrt{\Omega_\Lambda + \Omega_m(1+z)^3}$.

We proceed by modeling the CB intensity from different sources, such as decaying DM or stars.

A. ALP decay

We remain agnostic about the exact axion (axions in the following include ALPs) characteristics, but we assume that they are massive enough so that their main interaction is the decay to two photons through $g_{a\gamma}$, which entails a mass $m_a \gtrsim \mathcal{O}(\text{eV})$. The decay rate Γ_a , the inverse of the axion mean life τ_a , depends on the axion mass and coupling [45],

$$\begin{aligned} \Gamma_a = \tau_a^{-1} &= \frac{(m_a c^2)^3 g_{a\gamma}^2}{32h} \\ &= 7.56 \times 10^{-26} \text{s}^{-1} \left(\frac{m_a c^2}{\text{eV}} \right)^3 \left(\frac{g_{a\gamma}}{10^{-10} \text{GeV}^{-1}} \right)^2, \end{aligned} \quad (3)$$

with h being the Planck constant and c the speed of light in vacuum.

When an axion decays into two photons, the photons

are produced at a wavelength

$$\lambda_{\text{decay}} = hc \frac{2}{m_a c^2} = 2.48 \mu\text{m} \left(\frac{m_a c^2}{1 \text{ eV}} \right)^{-1}. \quad (4)$$

1. Cosmic axion decay

The main contribution we study comes from axions distributed throughout the Universe. The emissivity of cosmic axion decay is given by [57]

$$\varepsilon_{\lambda,a}(\lambda) = L_h \delta \left(\lambda - hc \frac{2}{m_a c^2} \right), \quad (5)$$

with L_h the axion luminosity density, which is the luminosity of an axion DM halo of mass M_h divided by the comoving number of halos n ,

$$\begin{aligned} L_h &= \frac{M_h c^2}{n \tau_a} = \Omega_a \rho_{\text{crit},0} \Gamma_a c^2 \\ &= 1.59 \times 10^{-34} \frac{\text{erg}}{\text{cm}^3 \text{ s}} \left(\frac{m_a c^2}{1 \text{ eV}} \right)^3 \left(\frac{g_{a\gamma}}{10^{-10} \text{ GeV}^{-1}} \right)^2. \end{aligned} \quad (6)$$

Assuming the distribution of halos to be homogeneous, we can relate these quantities to the mean axion density of the Universe $\rho_a = \Omega_a \rho_{\text{crit},0}$, with Ω_a the fraction of DM in the form of axions and $\rho_{\text{crit},0}$ the current critical matter density of the Universe.

The emissivity expression is technically not a Dirac δ function but a Gaussian distribution, where the width of the decay line is related to the nonrelativistic Doppler effect caused by the velocity dispersion of axions. This width will in general, be different in each system, e.g., in a galactic halo or galaxy cluster. The broadening is defined as

$$\sigma_{\text{decay}} = 2\lambda_{\text{decay}} \frac{v_{\text{disp}}}{c}, \quad (7)$$

where v_{disp} is the velocity dispersion of the bound axions. The typical velocity dispersion measured in galaxies is $v_{\text{disp}} \sim 100 - 300 \text{ km/s}$ [58, 59], which gives a ratio $\sigma_{\text{decay}}/\lambda_{\text{decay}} \lesssim 10^{-3}$. For the contribution to the CB, the ALP decay emissivity is integrated over redshift. In this case, given the small line width, it is safe to approximate the Gaussian line with a δ function. More details on this procedure can be found in Ref. [60].

We can plug in the emissivity given by Eq. (5) in Eq. (1) and obtain the axion decay contribution to the CB

$$\nu I_\nu(\lambda, z) = \frac{\Omega_a \rho_{\text{crit},0} c^4 (m_a c^2)^2 g_{a\gamma}^2}{64\pi \lambda H(z_*)} \Theta(z_* - z), \quad (8)$$

where

$$z_* = \frac{m_a c^2 \lambda}{2 hc} (1 + z) - 1. \quad (9)$$

We provide a more detailed derivation in Appendix A.

2. Local halo axion decay

So far, we have described the contribution that a homogeneous population of halos would give. As a complementary emission, we also take into account the DM decay in our local Milky Way halo. For this, we need to integrate the Galactic DM density over the line of sight through the DM halo. For this purpose, we use the software CLUMPY [61–63]. We define the DM column density S as the integral over the DM density along the line of sight (LOS) $\ell(\psi)$, which depends on the LOS angle $\psi(l, b)$ for Galactic longitude and latitude l, b ,

$$S(\psi) = \int_{\text{LOS}} d\ell \rho_{\text{DM}}(r(\psi)), \quad (10)$$

which has units GeV/cm^2 . For our purposes we have chosen a description of our DM halo with a Navarro-Frenk-White (NFW) profile [64]

$$\rho_{\text{DM}}(r) = \frac{\rho_\odot}{\frac{r}{r_s} \left(1 + \frac{r}{r_s} \right)^2}, \quad (11)$$

with values for the local DM density in the solar neighborhood $\rho_\odot = 0.42 \text{ GeV}/\text{cm}^3$, distance from the Sun to the Galactic Center $r_\odot = 8.275 \text{ kpc}$, virial radius $r_{\text{vir}} = 220 \text{ kpc}$, and scale radius $r_s = 21 \text{ kpc}$ [2, 65].

Since our CB measurements are compilations that encompass many regions of the sky, we use two different estimates for S that characterize the observations. The smallest possible S is the one that corresponds to a pointing in the Galactic anticenter, which we use as a conservative estimate. A more realistic value can be computed for the NH measurement. It was obtained from observations of different sky regions and observation times [40]. We opt for an average value of all pointings, weighted with the observation times. These two values are reported in Table I.

	Galactic coordinates (l, b)	S (GeV/cm^2)
Galactic antiCenter	($0^\circ, 180^\circ$)	1.11×10^{22}
LORRI observations	Table 2 of [40]	2.21×10^{22}

TABLE I: Values of S calculated for two relevant cases discussed in the text. An NFW profile is assumed, with DM halo parameters described in the text.

The flux coming from the DM decay is given by [61]

$$\begin{aligned} \frac{d\Phi}{dE d\Omega} &= \frac{1}{4\pi} \frac{\Gamma_a}{m_a c^2} \frac{dN_\gamma}{dE_\gamma} S \\ &= \frac{1}{4\pi} \frac{\Gamma_a}{m_a c^2} \frac{hc}{E^2} \frac{dN_\gamma}{d\lambda} S, \end{aligned} \quad (12)$$

where $dN_\gamma/dE_\gamma = hc/E^2 dN_\gamma/d\lambda$ is the spectrum of the axion decay, previously defined as a δ function. Here we

do not integrate dN_γ/dE_γ over wavelength, but rather consider its value at specific wavelengths. Therefore, we cannot use a δ -function approximation as in the cosmic case.¹ So for the local DM decay contribution, we do account for broadening due to velocity dispersion [57]

$$\frac{dN_\gamma}{d\lambda}(\lambda, \lambda_{\text{decay}}) = \frac{1}{\sqrt{2\pi}\sigma_{\text{decay}}} e^{-\frac{1}{2}\left(\frac{\lambda - \lambda_{\text{decay}}}{\sigma_{\text{decay}}}\right)^2}, \quad (13)$$

Plugging in Γ_a from Eq. (3), the broadening from Eq. (7) and the definition of Eq. (13), we find for the intensity

$$\begin{aligned} \nu I_\nu(\lambda) &= E^2 \frac{d\Phi}{dE d\Omega} \\ &= \frac{c(m_a c^2)^3}{512\pi \sqrt{2\pi} h v_{\text{disp}}} g_{a\gamma}^2 S e^{-\frac{1}{2}\left(\frac{\lambda - \lambda_{\text{decay}}}{\sigma_{\text{decay}}}\right)^2} \\ &= 14.53 \frac{\text{nW}}{\text{sr m}^2} \left(\frac{m_a c^2}{1\text{eV}}\right)^3 \left(\frac{g_{a\gamma}}{10^{-10}\text{GeV}^{-1}}\right)^2 \\ &\quad \times \left(\frac{S}{1.11 \times 10^{22}\text{GeVcm}^{-2}}\right) \left(\frac{v_{\text{disp}}}{220\text{km/s}}\right)^{-1} \\ &\quad \times e^{-\frac{1}{2}\left(\frac{\lambda - \lambda_{\text{decay}}}{\sigma_{\text{decay}}}\right)^2}. \end{aligned} \quad (14)$$

B. Astrophysical sources of the CB

1. Model of COB

The excess observed with LORRI could be due to a combination of astrophysical COB emission and ALP decay. The publicly available models of the COB usually share only their final results, without providing the means to change the input parameters or add additional sources. Since we aim to study how much additional COB emissivity astrophysical models and additional sources would allow, we develop our own COB model. This allows us to investigate whether it is possible to ease the tension between the COB lower limits and the LORRI measurements and to investigate potential degeneracies between the ALP and astrophysical contributions. As we will see below, the stellar COB contribution is completely fixed by the observations of galaxy emissivities, erasing any such degeneracy.

The COB is dominated by stellar emission, which is partly absorbed by interstellar dust. Other known astrophysical components include AGN emission which, however, dominates in the ultraviolet and accounts for at most 10% of the COB [48, 66], or intrahalo light, whose contribution is expected to be negligible [45, 67, 68].

For our COB model, we follow the methodology of Ref. [48], hereafter *Finke22*. Synthetic stellar spectra are calculated with the *STARBURST99* code [69, 70], using a

Kroupa initial mass function (IMF) with $M_{\text{min}} = 0.1 M_\odot$ and $M_{\text{max}} = 100 M_\odot$ [71]. We maintain the dust and star formation rate parametrizations used in Ref. [48], but parametrize the metallicity evolution following Ref. [72]. We fit our model to various datasets of COB intensity, stellar emissivities, star formation rate, and metallicities [37, 38, 48, 73, 74], obtaining a reduced χ^2 value over degrees of freedom of $\chi^2/\text{d.o.f.} = 2.7$. Adding these datasets to the COB fit essentially fixes the stellar contribution, as the introduction of the ALP decay to the CB does not affect the metallicity, star formation rate, and galaxy emissivities. As a consequence, we choose to fix the COB contribution to its best fit and add additional contributions such as ALP decay on top of it. We also tested adding other components (intrahalo light, stripped stars) to check whether their contributions could help explain the LORRI excess. However, these other contributions are not bright enough and we can rule them out as possible sources for the excess.

This model is shown in Fig. 1. Further details about this model and tests with different contributions are detailed in Appendix B.

We use two preexisting COB models to compare with ours. The first one comes from *Finke22*, which encompasses the COB and CIB and models the contributions of stars and dust. The second one is the model of Ref. [49], hereafter *CUBA*, which covers the frequency range from the CXB to the COB and models all the dominant processes of radiative transfer. They are both shown in Fig. 1. In the central region of the COB, the model with the smallest intensity is *CUBA*; while at the smaller COB wavelengths it is *Finke22*. These behaviors are also shown in the top part of Fig. 2.

2. Model of CUB and CXB

The main components of the CUB are emission from young stars and interstellar nebulae, scattered by gas and hot intercluster gas [37]. The efficiency of neutral hydrogen of absorbing ultraviolet light is almost unity [37], which results in a very low intensity of the CUB compared to the COB, see Fig. 1.

The CXB is mainly produced by accretion disks around AGN, which create high-energy photons via thermal Bremsstrahlung effect [37].

In contrast to the COB, we solely rely on the *CUBA* predictions for the CUB and CXB.

IV. DATA ANALYSIS

To constrain the axion parameters, we treat the (putative) direct detections of the CB as one-sided upper limits. Under the assumption that the likelihoods for the

¹ The value of the flux would be infinite at a certain wavelength.

data points follow Gaussian statistics, we arrive at

$$\chi^2 = \sum_i \left(\frac{\nu I_{\nu_{\text{model}}}(\lambda_i) - \nu I_{\nu_i}}{\sigma_i} \right)^2 \times \Theta(\nu I_{\nu_{\text{model}}}(\lambda_i) - \nu I_{\nu_i}), \quad (15)$$

where $\Theta(x)$ is the Heaviside step function, and $\nu I_{\nu_{\text{model}}}$ is the sum of the CB and axion decay contribution. The CB contribution is fixed by either the predictions of the [CUBA](#) or [Finke22](#) models, or the predictions from our own model. The latter is, in turn, fixed by the fit to various datasets as described in [Appendix B](#).

For the COB upper limits and CUB putative measurements we take the value of $\nu I_{\nu_{\text{model}}}$ as the value given by the model at the given wavelength λ_i , but for the CXB measurements we calculate the mean value of νI_{ν} over each energy bin.

Alternatively, we treat the NH data point as a measurement. In this case, we take the LORRI quantum efficiency $P(\lambda)$ into account. The wavelength dependence of $P(\lambda)$ is given in [Fig. 22](#) of [Ref. \[75\]](#). This is necessary as the spectral shape of the axion decay signal is not flat, as was assumed for the measurement of the COB. The mean flux measured over the detector is given by

$$I_{\nu, \text{mean}} = \frac{\int I_{\nu}(\lambda) P(\lambda) d\lambda/\lambda}{\int P(\lambda) d\lambda/\lambda}. \quad (16)$$

The term $I_{\nu}(\lambda)$ is the spectral intensity measured with LORRI, which in our case is the sum of astrophysical COB and axion decay. This expression is taken from [Ref. \[76\]](#), but we have used intensities in the calculations instead of flux. Intensity I_{ν} and flux f_{ν} are related by the integration over solid angle and since I_{ν} is isotropic, it does not matter if we use intensity or flux. Furthermore, the mean wavelength associated with this flux measurement is given by [\[76\]](#)

$$\langle \lambda \rangle = \frac{\int P(\lambda) I_{\nu}(\lambda) d\lambda}{\int P(\lambda) I_{\nu}(\lambda) d\lambda/\lambda}. \quad (17)$$

With axion decay present in the wavelength range of the bandpass, both the mean intensity and wavelength depend on m_a and $g_{a\gamma}$.

With these considerations, we can now compare our model predictions with the LORRI measurement through

$$\chi^2 = \left(\frac{\nu I_{\nu_{\text{mean, model}}}(\langle \lambda \rangle) - \nu I_{\nu, \text{NH}} \times \lambda_{\text{pivot}}/\langle \lambda \rangle}{\sigma_{\text{NH}}} \right)^2, \quad (18)$$

where $\lambda_{\text{pivot}} = 0.6076 \mu\text{m}$ is the pivot wavelength of the LORRI bandpass associated with the LORRI measurement [\[75\]](#). The ratio $\lambda_{\text{pivot}}/\langle \lambda \rangle$ comes from shifting the NH measurement to the same mean wavelength as our calculation, so we can perform a consistent comparison.

V. RESULTS

We first discuss the results for cosmic axion decay, followed by the results for axion decay in the local halo, and finally the results for the LORRI measurement.

A. Cosmic axions

We add the cosmic axion component given in [Eq. \(8\)](#) to the COB models and explore the axion-photon coupling parameter space for which the axion contribution does not overshoot the CB upper limits. An example of axion decay added to the [CUBA](#) model, with arbitrary values for the axion parameters, can be seen in [Fig. 1](#).

Treating the NH data point as an upper limit, along with the other upper limits, we follow the methodology in [Eq. \(15\)](#) and calculate exclusions at the 2σ confidence level. In [Fig. 2](#) we show our constraints derived from COB data (bottom panel) and an enlargement of the COB measurements themselves (top panel). In the upper (lower) panel, the upper (lower) x axis shows the axion mass, which is related to wavelength through [Eq. \(4\)](#). One can observe a correspondence between the constraints and the COB data points: for upper limits of comparatively low intensity (such as the [AKARI/IRC \[77\]](#) or the [Dark Cloud measurements \[78\]](#)), the limits improve toward higher axion masses and result in sharp features. We have used the LORRI measurement of [\[40\]](#) for the calculations, but this value has little relevance, since the constraints in that region are dominated by the [Dark Cloud measurements](#). There is a sharp cut in the constraints at higher wavelengths since the parameter space we can scan with this methodology ends at the position of the highest wavelength data point we consider. Note that lower decay wavelengths correspond to higher axion masses, and the tails in the decay spectra of these axions (see [Fig. 1](#) for an example) also contribute to the χ^2 . The different COB models result in very similar axion constraints.

In [Fig. 3](#) we show the constraints of the axion-photon coupling for the full wavelength range we consider, again using the methodology of [Eq. \(15\)](#). We have calculated this set of constraints using the [CUBA](#) model as the astrophysical contribution, adding the cosmic axion decay on top. Using only the data points from the COB, CUB, and the CXB, we arrive at the constraints shown as filled blue, yellow, and pink regions, respectively. These constraints are at 2σ confidence. The constraint from the whole spectral region, using all the data points, is shown as the white line. We guide the figure with a green straight line labeled $\tau = 4.5 \times 10^{17}\text{s}$, which links the axion parameters following [Eq. \(3\)](#) using the age of the Universe [\[1\]](#) as the mean axion lifetime. For all the filled regions we can observe a power-law behavior of the constraints toward higher masses. This is due to the definition of our χ^2 function and further detailed in [Appendix C](#).

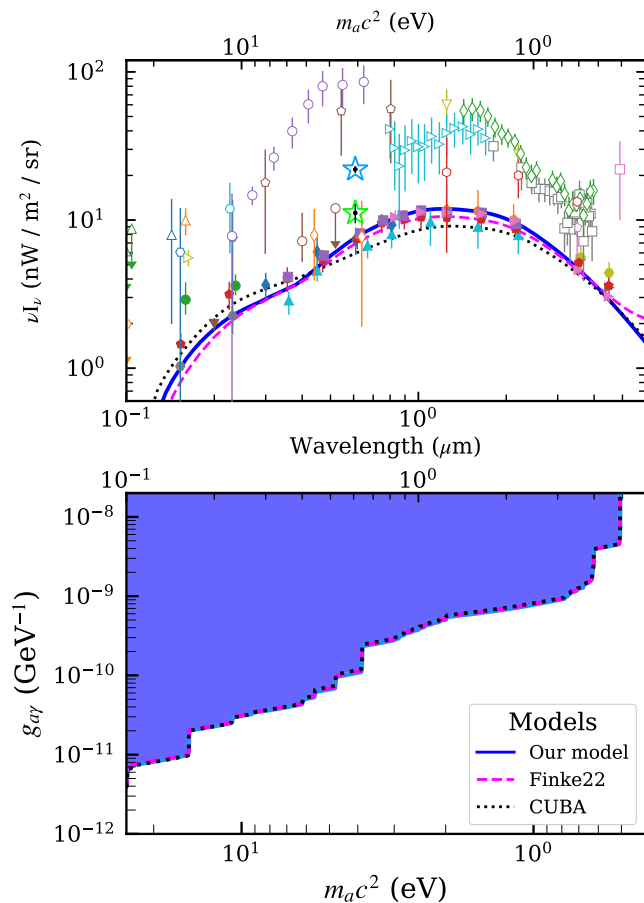


FIG. 2: Top: COB measurements and models used or calculated in this work. Bottom: axion parameter space that is constrained by the COB upper limits by considering the cosmic axion contribution (for each of the discussed COB models). The excluded region (at a 2σ confidence level) is above the different lines, shaded in blue. Note the descending x axis, following the correlation between axion mass and photon wavelength in Eq. (4).

B. Decay in the Galactic halo

Next, we consider the axion decay contribution from the local Milky Way halo, given by Eq. (14).

We start with the addition of the host axion decay in the wavelength bands of the COB and CUB. The observations at these wavelengths have been carried out on a large variety of instruments with different bandpasses using different data analysis techniques. For simplicity, we opt to use the measured intensities at face value and at the reported wavelengths, i.e., we neglect the finite bandpass, which we only consider in the case of the LORRI measurements. Incorporating the specific instrumental responses is left for future study.

In Fig. 4 we show examples of the decay of an axion with masses between $m_a = 3$ and 8 eV including

both cosmic and host contributions on top of the CUBA model. The coupling constant is the same for all considered masses. We can see that the host contribution is only relevant at wavelengths corresponding to energies at half of the axion rest mass, whereas the cosmic decay contribution dominates the decay spectrum at longer wavelengths. Therefore, the Galactic halo decay mostly affects the constraints close to the corresponding wavelengths at which we have measurements.

We consider the single data points one at a time. For each data point, we calculate the axion mass that would contribute to the intensity following Eq. (4) and then the $\nu I_{\nu_{\text{model}}}$ necessary to overshoot the 2σ uncertainty using Eq. (15). We determine the corresponding coupling constant following Eqs. (8) and (14). We use the column density S from the Galactic anticenter, yielding conservative constraints. The only exception is the LORRI observation, for which we use the values for S listed in Table I. The result is plotted in Fig. 3 as the black line, where we can see sudden dips departing from the white line in the COB and CUB at axion masses where we have a data point at the correct wavelength.

In the CXB region, we perform a similar analysis, but we include the widths in wavelength of the spectral data points. Instead of assuming a monochromatic decay and only checking the flux on the associated wavelength, we calculate the mean value of the intensity of the axion decay in each bin and use this value for our model estimate $\nu I_{\nu_{\text{model}}}$. We assume a constant exposure in each wavelength bin. This results in constraints in the CXB that are not as sharp as in the COB and CUB, see the black line in Fig. 1.

C. Analysis of LORRI observations

Finally, we turn our attention to the LORRI measurement. In this analysis, we make use of the quantum efficiency and finite bandpass of the detector and find the axion parameters for which the CUBA model and axion contributions fit the NH data point. To this end, we first calculate the mean flux and wavelength of the axion decay spectrum following Eqs. (16) and (17), respectively. The quantum efficiency of the LORRI instrument is shown in Fig. 4 as a gray line (see the right y axis). The pivot wavelength of the detector is shown as the vertical black line. As mentioned before, in this figure, we also show examples of axion decay spectra for different masses. For these spectra we calculate their associated mean wavelength with Eq. (17) (dotted vertical lines) and the corresponding mean flux with Eq. (16) (black dots and colored diamonds). The spectrum, mean wavelength, and flux for each axion mass share the same color. We can see that the mean wavelength varies with mass and we show this dependency in Fig. 5 for a fixed photon-axion coupling and the CUBA model. Compared to the pivot wavelength (gray dashed line), which corresponds to a flat spectrum, we see several features in

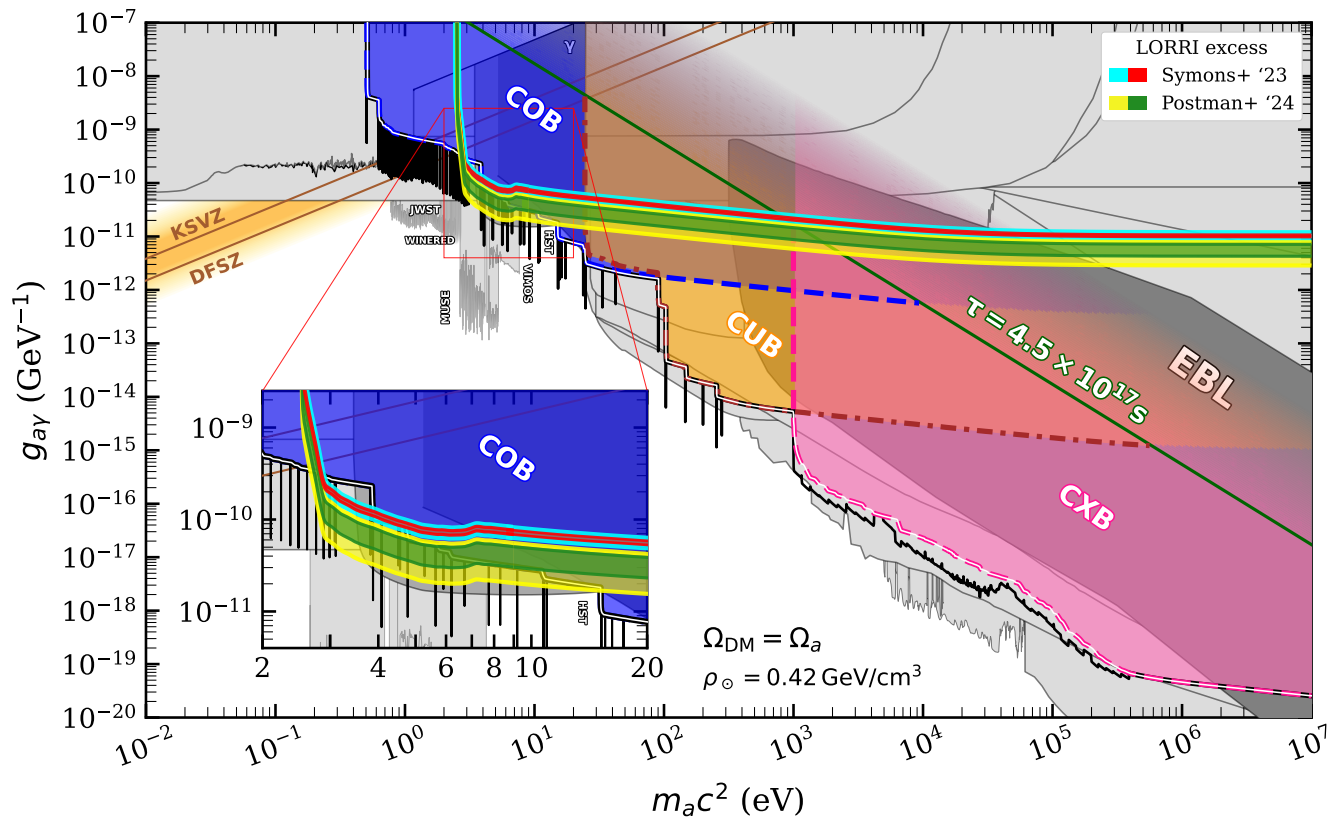


FIG. 3: Our and previous constraints on the axion and ALP parameter space, using the **CUBA** model. Confidence intervals at 1σ (2σ) that could explain the NH excess are shown in red (blue) for the values of Ref. [40] and in green (yellow) for the values of Ref. [46]. Constraints at 2σ confidence using the NH measurement from [40] as an upper limit, together with the rest of upper limits from Fig. 1, are shown as shaded blue, yellow, and pink regions for the COB, CUB, and CXB, respectively. The inset shows the comparison between COB models in Fig. 1. The black line shows the overall constraint when also the axion decay in the local DM halo is accounted for. Limits from previous analyses are depicted in gray and are taken from the compilation of Ref. [79].

the mean wavelengths, in particular when the host decay is included (orange and green lines). These features stem from the sharply peaked decay spectrum folded with the LORRI quantum efficiency. At high and low masses, when the decay peak is not within the LORRI passband anymore, we still observe a shift of the mean wavelength compared to the pivot wavelength, which is due to the **CUBA** model itself.

Having the mean wavelength and flux, we calculate the χ^2 value from Eq. (18). In Fig. 3, we show the 1σ and 2σ confidence intervals (corresponding to a $\Delta\chi^2 = 2.30, 5.99$ for 2 degrees of freedom) of the axion parameters that would explain the LORRI measurements of Ref. [40] (Ref. [46]) in red and blue (green and yellow). The preferred coupling constant lies between 10^{-10} and $10^{-11} \text{ GeV}^{-1}$ for masses above $m_a \gtrsim 2 \text{ eV}$. The preferred regions for the two LORRI measurements have the same shape, the difference between them being the strength of coupling necessary to obtain the excess value.

In the inset of Fig. 3, we show an enlarged view of the axion constraints in the COB regime. In this re-

gion, also the DM host decay contributes to the LORRI measurement up to roughly $m_a \sim 7 \text{ eV}$, which can be seen in the shape of the confidence intervals. In this region, up to $m_a \sim 10 \text{ eV}$, axions could both explain the NH excess and not violate the other CB upper limits. However, this region has been excluded by other experiments such as the observations of globular clusters [80], spectroscopic searches with the Multi Unit Spectroscopic Explorer (MUSE) [34] or study of COB anisotropies with the Hubble Space Telescope (HST) [35].

VI. DISCUSSION

We find that the different COB models provide very similar constraints in the axion parameter space, as we see in Fig. 2. Thanks to the implementation of our own COB model, detailed in Appendix B, we test different characterizations of the stellar population, such as stellar spectra or dust descriptions. Our best-fit model still has a reduced χ^2 value larger than unity, its largest contribu-

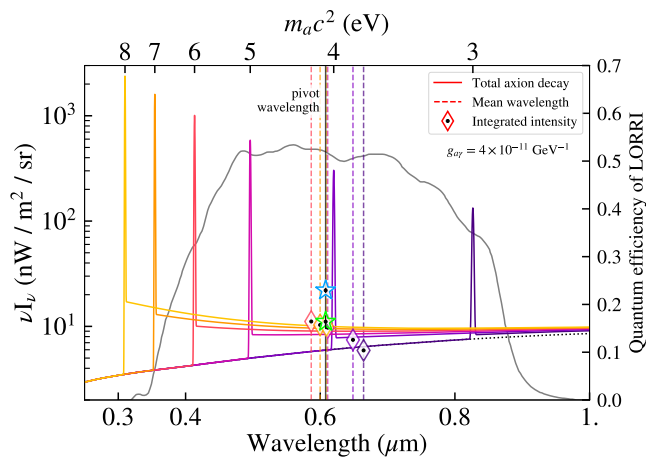


FIG. 4: Cosmic and local axion decay spectra for axions at different masses. The mean wavelength of each spectrum is shown as a vertical line sharing the color of each axion spectrum calculated with Eq. (17), as well as the mean flux from Eq. (16). The dotted line is the CUBA spectrum. The gray line and the right y axis give the quantum efficiency of the LORRI detector.

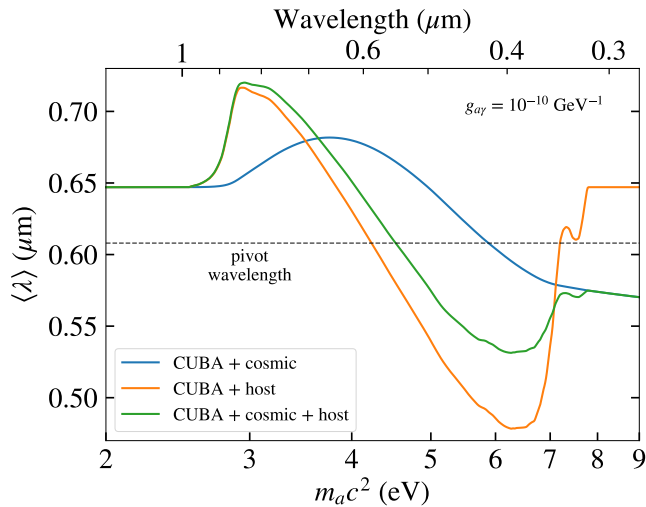


FIG. 5: Mean wavelength associated with axion decays, as a function of axion mass following Eq. (17) assuming constant coupling constant.

tion coming from the fit to stellar emissivities. We find that the best-fit COB model is completely fixed by the observational data, leaving no room for altering its spectrum significantly to potentially relieve tension with the LORRI data point. We also find that other astrophysical contributions to the COB such as AGN, intrahalo light, or a population of stars with stripped envelopes are subdominant, see Appendix B 5. Looking at Fig. 3, we see that only a small region of the axion parameter space, located at $m_a \sim 4 - 5$ eV, could explain the NH data point, while simultaneously not overshooting other

CB upper limits. As mentioned before, this parameter space is ruled out by other experiments such as globular clusters [80] or MUSE [34].

Previous limits that use a similar technique as ours are shown in dark gray in Fig. 3. In particular, Ref. [30], labeled “EBL” in the figure, also used the CB spectrum available at that time to constrain axion parameters. Our constraints improve their results by 1 order of magnitude over a wide range of axion masses, also extending it to lower masses. We even rule out the Dine-Fischler-Srednicki-Zhitnitsky (DFSZ) and Kim-Vainshtein-Shifman-Zakhar (KVSZ) axion models in between $m_a = 2$ and 30 eV. Our results are more restrictive because we include the latest CB measurements and the astrophysical contribution to the CB. Limits labeled HST [81] and γ [45] are based on the NH measurement as well but different methodologies were used for their derivation. For the HST constraint, it was studied how the LORRI excess impacts COB anisotropy. The γ exclusion used the axion contribution to the COB in the resulting increase to the optical depth for very high-energy γ rays. Our results yield, in general, similar constraints compared to these studies. We extend the analysis by Ref. [44] by including additional CB measurements in our analysis. As a consequence, only a small region of the axion parameter space is allowed to explain the LORRI data point.

Further constraints in the $m_a \sim 1 - 10$ eV regime, such as MUSE [34], Visible Multiobject Spectrograph [33], and James Webb Space Telescope (JWST) [31] as labeled in Fig. 3, stem from spectroscopic measurements. This method proves to be more constraining compared to our analysis, while also being more restricted by the detection range of instruments.

VII. SUMMARY AND CONCLUSIONS

In this work we have investigated the impact of axion or ALP decay on the CB, specifically from optical wavelengths to x-ray energies. We have put particular emphasis on the optical regime due to the tentative excess observed with LORRI [40], on board the NH probe, although latest measurements suggest it is not significant anymore [46]. Such an excess would be challenging to explain with known astrophysical sources.

To this end, we have implemented our own COB model. We have tested various model assumptions by fitting them to observational data and have found our best-fit model, which we show in the main text. We compare our results with those of Finke22 and CUBA and find that different COB models provide similar results. Specifically, when applying these models to the axion decay, the constraints are very similar.

Concerning the axion-photon parameter space, we find only a small region of the parameter space around $4 - 5 \mu\text{m}$ can explain the NH point as a direct measurement of the CB while not overshooting the CB upper

limits. This parameter space has been ruled out by other experiments. We also find that this mild excess is unlikely caused by either intrahalo light or stripped stars. As we show in Appendix B 5, intrahalo light peaks at wavelengths above the LORRI bandpass, and stripped stars contribute around 1% to the COB. However, we note again that the significance of the excess is only at 1.4σ above the COB level measured with galaxy counts. The parameter space that explains the excess reported in Ref. [40] is fully constrained by other experiments. We have also calculated new constraints in the axion-photon parameter space assuming the NH observation as another upper limit, and combined its analysis to a compilation of CB measurements. Our constraints improve the previous ones from Ref. [30] on average by a factor of 10 (see Fig. 3). Assuming $\Omega_a = \Omega_{\text{DM}}$, we rule out the DFSZ and KVSZ axion models in between $m_a = 2$ and 30 eV with the decay of cosmic axions.

Axion decay in the Galactic halo would create narrow peaks of flux in the COB and CUB. This leads to strong constraints at axion masses corresponding to a wavelength where CB measurements are available. In the CXB, the effect is less striking, as we have averaged the signal over each energy bin (see Fig. 3). For the constraints we conservatively assumed the DM column density S of the Galactic anticenter, which is insensitive to the adopted DM profile and scales linearly with the assumed DM density in the Solar System (we used $\rho_{\odot} = 0.42 \text{ GeV/cm}^3$). There is one exception to this: for the NH measurements, we calculated the weighted mean of S , based on the observation times and pointings of the probe.

As an outlook, new measurements of the CB, i.e. with the JWST, would improve our predictions: both direct

and indirect measurements of the CB, as well as better characterization of stellar parameters. Moreover, further sources could contribute to the CB. For example, a change in the stellar formation rate at high redshift due to primordial black holes [82] or the existence of Population III stars [83] would increase the astrophysical CB component. Another source could be dark stars [84]. The decay in the local halo is another sensitive probe. Detailed analysis with correct values of the DM column density S for each observation could be promising, which we aim to explore in a future publication. Furthermore, we plan to extend our analysis to higher energies and include the extragalactic diffuse γ -ray background, and lower energies to account for the infrared background.

ACKNOWLEDGMENTS

The authors would like to thank Ciaran O’Hare for his thoughtful comments and discussions. We would also like to thank Todd Lauer and Marc Postman for sharing the preliminary updated LORRI measurement. We further thank Marco Ajello and Kari Helgason for providing us with the data of the SFR in machine-readable format. The authors acknowledge support from the European Research Council (ERC) under the European Union’s Horizon2020 research and innovation program Grant Agreement No. 948689 (AxionDM) and from the Deutsche Forschungsgemeinschaft (DFG, German Research Foundation) under Germany’s Excellence Strategy – EXC 2121 “Quantum Universe”– 390833306. This article is based upon work from COST Action COSMIC WISPerS CA21106, supported by COST (European Cooperation in Science and Technology).

-
- [1] Planck Collaboration, N. Aghanim, Y. Akrami, *et al.*, Planck 2018 results. VI. Cosmological parameters, *A&A* **641**, A6 (2020), arXiv:1807.06209 [astro-ph.CO].
 - [2] S. Navas, C. Amsler, T. Gutsche, *et al.* (Particle Data Group Collaboration), Review of particle physics, *Phys. Rev. D* **110**, 030001 (2024).
 - [3] J. Preskill, M. B. Wise, and F. Wilczek, Cosmology of the invisible axion, *Physics Letters B* **120**, 127 (1983).
 - [4] M. Dine and W. Fischler, The not-so-harmless axion, *Physics Letters B* **120**, 137 (1983).
 - [5] R. D. Peccei and H. R. Quinn, CP conservation in the presence of pseudoparticles, *Physical Review Letters* **38**, 1440 (1977), aDS Bibcode: 1977PhRvL..38.1440P.
 - [6] R. D. Peccei and H. R. Quinn, Constraints imposed by CP conservation in the presence of pseudoparticles, *Physical Review D* **16**, 1791 (1977), aDS Bibcode: 1977PhRvD..16.1791P.
 - [7] I. G. Irastorza and J. Redondo, New experimental approaches in the search for axion-like particles, *Progress in Particle and Nuclear Physics* **102**, 89 (2018), arXiv:1801.08127 [hep-ph].
 - [8] P. Arias, D. Cadamuro, M. Goodsell, J. Jaeckel, J. Redondo, and A. Ringwald, WISPy cold dark matter, *J. Cosmology Astropart. Phys.* **2012**, 013 (2012), arXiv:1201.5902 [hep-ph].
 - [9] C. P. Salemi, J. W. Foster, J. L. Ouellet, A. Gavin, K. M. W. Pappas, S. Cheng, K. A. Richardson, R. Henning, Y. Kahn, R. Nguyen, N. L. Rodd, B. R. Safdi, and L. Winslow, The search for low-mass axion dark matter with ABRACADABRA-10cm, *Physical Review Letters* **127**, 081801 (2021), arXiv:2102.06722 [hep-ex, physics:hep-ph].
 - [10] T. A. Collaboration, S. J. Asztalos, G. Carosi, C. Hagmann, D. Kinion, K. van Bibber, M. Hotz, L. Rosenberg, G. Rybka, J. Hoskins, J. Hwang, P. Sikivie, D. B. Tanner, R. Bradley, and J. Clarke, A SQUID-based microwave cavity search for dark-matter axions, *Physical Review Letters* **104**, 041301 (2010), arXiv:0910.5914 [astro-ph].
 - [11] C. M. Adair, K. Altenmüller, V. Anastassopoulos, *et al.*, Search for Dark Matter Axions with CAST-CAPP, *Nature Communications* **13**, 6180 (2022), arXiv:2211.02902 [hep-ex].
 - [12] D. Alesini, D. Babusci, C. Braggio, *et al.*, Search for galactic axions with a high-Q dielectric cavity, *Physical*

- Review D **106**, 052007 (2022), arXiv:2208.12670 [hep-ex, physics:physics].
- [13] V. Anastassopoulos, S. Aune, K. Barth, *et al.*, New CAST limit on the axion-photon interaction, *Nature Physics* **13**, 584 (2017), arXiv:1705.02290 [hep-ex].
- [14] M. Betz, F. Caspers, M. Gasior, M. Thumm, and S. W. Rieger, First results of the CERN Resonant WISP Search (CROWS), *Physical Review D* **88**, 075014 (2013), arXiv:1310.8098 [physics].
- [15] R. Ballou, G. Deferne, M. Finger Jr., M. Finger, L. Flekova, J. Hosek, S. Kunc, K. Macuchova, K. A. Meissner, P. Pugnati, M. Schott, A. Siemko, M. Slunceka, M. Sulc, C. Weinsheimer, and J. Zicha, New Exclusion Limits for the Search of Scalar and Pseudoscalar Axion-Like Particles from "Light Shining Through a Wall", *Physical Review D* **92**, 092002 (2015), arXiv:1506.08082 [hep-ex, physics:physics].
- [16] F. Della Valle, E. Milotti, A. Ejlli, U. Gastaldi, G. Messineo, G. Zavattini, R. Pengo, and G. Ruoso, The PVLAS experiment: measuring vacuum magnetic birefringence and dichroism with a birefringent Fabry-Perot cavity, *The European Physical Journal C* **76**, 24 (2016), arXiv:1510.08052 [hep-ex, physics:physics, physics:quant-ph].
- [17] Y. Kiritu, T. Hasada, M. Hashida, Y. Hirahara, K. Homma, S. Inoue, F. Ishibashi, Y. Nakamiya, L. Neagu, A. Nobuhiro, T. Ozaki, M.-M. Rosu, S. Sakabe, and O. Tesileanu, *Search for sub-eV axion-like particles in a stimulated resonant photon-photon collider with two laser beams based on a novel method to discriminate pressure-independent components* (2022), arXiv:2208.09880 [hep-ex].
- [18] G. Atlas Collaboration, Aad, B. Abbott, D. C. Abbott, *et al.*, Measurement of light-by-light scattering and search for axion-like particles with 2.2 nb^{-1} of Pb+Pb data with the ATLAS detector, *Journal of High Energy Physics* **2021**, 243 (2021), arXiv:2008.05355 [hep-ex].
- [19] F. Abudinén, I. Adachi, H. Aihara, N. Akopov, A. Aloisio, *et al.*, Search for Axionlike Particles Produced in e^+e^- Collisions at Belle II, *Phys. Rev. Lett.* **125**, 161806 (2020).
- [20] A. M. Sirunyan, A. Tumasyan, W. Adam, *et al.*, Evidence for light-by-light scattering and searches for axion-like particles in ultraperipheral PbPb collisions at $\sqrt{s_{NN}} = 5.02 \text{ TeV}$, *Physics Letters B* **797**, 134826 (2019), arXiv:1810.04602 [hep-ex].
- [21] D. Aloni, C. Fanelli, Y. Soreq, and M. Williams, Photoproduction of axion-like particles, *Physical Review Letters* **123**, 071801 (2019), arXiv:1903.03586 [hep-ex, physics:hep-ph, physics:nucl-ex].
- [22] P. Astier, D. Autiero, A. Baldisseri, M. Baldo-Ceolin, *et al.*, Search for eV (pseudo)scalar penetrating particles in the SPS neutrino beam, *Physics Letters B* **479**, 371 (2000).
- [23] S. Knapen, T. Lin, H. K. Lou, and T. Melia, Searching for axion-like particles with ultra-peripheral heavy-ion collisions, *Physical Review Letters* **118**, 171801 (2017), arXiv:1607.06083 [hep-ex, physics:hep-ph].
- [24] K. Kohri and H. Kodama, Axion-Like Particles and Recent Observations of the Cosmic Infrared Background Radiation, *Physical Review D* **96**, 051701 (2017), arXiv:1704.05189 [astro-ph, physics:hep-ph, physics:hep-th].
- [25] A. Caputo, H.-T. Janka, G. Raffelt, and E. Vitagliano, Low-Energy Supernovae Severely Constrain Radiative Particle Decays, *Physical Review Letters* **128**, 221103 (2022), arXiv:2201.09890 [astro-ph, physics:hep-ph].
- [26] M. A. Buen-Abad, J. Fan, and C. Sun, *Constraints on Axions from Cosmic Distance Measurements* (2022), arXiv:2011.05993 [astro-ph, physics:hep-ph].
- [27] H.-J. Li, J.-G. Guo, X.-J. Bi, S.-J. Lin, and P.-F. Yin, Limits on axion-like particles from Mrk 421 with 4.5-year period observations by ARGO-YBJ and Fermi-LAT, *Physical Review D* **103**, 083003 (2021), arXiv:2008.09464 [astro-ph].
- [28] C. Dessert, A. J. Long, and B. R. Safdi, No evidence for axions from Chandra observation of magnetic white dwarf, *Physical Review Letters* **128**, 071102 (2022), arXiv:2104.12772 [astro-ph, physics:hep-ph].
- [29] F. Calore, P. Carena, C. Eckner, T. Fischer, M. Giannotti, J. Jaeckel, K. Kotake, T. Kuroda, A. Mirizzi, and F. Sivo, 3D template-based *Fermi*-LAT constraints on the diffuse supernova axion-like particle background, *Physical Review D* **105**, 063028 (2022), arXiv:2110.03679 [astro-ph, physics:hep-ph].
- [30] D. Cadamuro and J. Redondo, Cosmological bounds on pseudo Nambu-Goldstone bosons, *Journal of Cosmology and Astroparticle Physics* **2012**, 032, aDS Bibcode: 2012JCAP...02..032C.
- [31] R. Janish and E. Pinetti, *Hunting Dark Matter Lines in the Infrared Background with the James Webb Space Telescope* (2023), arXiv:2310.15395 [hep-ph].
- [32] D. Wadekar and Z. Wang, Strong constraints on decay and annihilation of dark matter from heating of gas-rich dwarf galaxies, *Physical Review D* **106**, 075007 (2022), arXiv:2111.08025 [astro-ph, physics:hep-ph].
- [33] D. Grin, G. Covone, J.-P. Kneib, M. Kamionkowski, A. Blain, and E. Jullo, A Telescope Search for Decaying Relic Axions, *Physical Review D* **75**, 105018 (2007), arXiv:astro-ph/0611502.
- [34] E. Todarello, M. Regis, J. Reynoso-Cordova, M. Taoso, D. Vaz, J. Brinchmann, M. Steinmetz, and S. L. Zoutendijk, *Robust bounds on ALP dark matter from dwarf spheroidal galaxies in the optical MUSE-Faint survey* (2023), arXiv:2307.07403 [astro-ph, physics:hep-ph].
- [35] P. Carena, G. Lucente, and E. Vitagliano, Probing the Blue Axion with Cosmic Optical Background Anisotropies, *Physical Review D* **107**, 083032 (2023), arXiv:2301.06560 [astro-ph, physics:hep-ph].
- [36] F. Calore, A. Dekker, P. D. Serpico, and T. Siebert, Constraints on light decaying dark matter candidates from 16 years of INTEGRAL/SPI observations, *Monthly Notices of the Royal Astronomical Society* **520**, 4167 (2023), arXiv:2209.06299 [astro-ph, physics:hep-ph].
- [37] R. Hill, K. W. Masui, and D. Scott, *The Spectrum of the Universe* (2018), arXiv:1802.03694 [astro-ph].
- [38] J. Biteau, *The multi-messenger extragalactic spectrum* (2023).
- [39] T. R. Lauer, M. Postman, J. R. Spencer, H. A. Weaver, *et al.*, Anomalous Flux in the Cosmic Optical Background Detected with New Horizons Observations, *The Astrophysical Journal Letters* **927**, L8 (2022), publisher: The American Astronomical Society.
- [40] T. Symons, M. Zemcov, A. Cooray, C. Lisse, and A. R. Poppe, A Measurement of the Cosmic Optical Background and Diffuse Galactic Light Scaling from the R_j 50 au New Horizons-LORRI Data, *ApJ* **945**, 45 (2023), arXiv:2212.07449 [astro-ph.CO].

- [41] M. G. Hauser, R. G. Arendt, T. Kelsall, E. Dwek, N. Odegard, J. L. Weiland, H. T. Freudenreich, W. T. Reach, R. F. Silverberg, S. H. Moseley, Y. C. Pei, P. Lubin, J. C. Mather, R. A. Shafer, G. F. Smoot, R. Weiss, D. T. Wilkinson, and E. L. Wright, The COBE Diffuse Infrared Background Experiment Search for the Cosmic Infrared Background. I. Limits and Detections, *ApJ* **508**, 25 (1998), [arXiv:astro-ph/9806167 \[astro-ph\]](#).
- [42] S. P. Driver, S. K. Andrews, L. J. Davies, A. S. G. Robotham, A. H. Wright, R. A. Windhorst, S. Cohen, K. Emig, R. A. Jansen, and L. Dunne, Measurements of Extragalactic Background Light from the Far UV to the Far IR from Deep Ground- and Space-based Galaxy Counts, *The Astrophysical Journal* **827**, 108 (2016), aDS Bibcode: 2016ApJ...827..108D.
- [43] R. A. Windhorst, S. H. Cohen, R. A. Jansen, J. Summers, S. Tompkins, C. J. Conselice, S. P. Driver, H. Yan, D. Coe, B. Frye, N. Grogan, A. Koekemoer, M. A. Marshall, *et al.*, JWST PEARLS. Prime Extragalactic Areas for Reionization and Lensing Science: Project Overview and First Results, *The Astronomical Journal* **165**, 13 (2023).
- [44] J. L. Bernal, G. Sato-Polito, and M. Kamionkowski, Cosmic Optical Background Excess, Dark Matter, and Line-Intensity Mapping, *Physical Review Letters* **129**, 231301 (2022).
- [45] J. L. Bernal, A. Caputo, G. Sato-Polito, J. Mirocha, and M. Kamionkowski, *Seeking dark matter with γ -ray attenuation* (2022), [arXiv:2208.13794 \[astro-ph, physics:hep-ph\]](#).
- [46] M. Postman, T. R. Lauer, J. W. Parker, J. R. Spencer, H. A. Weaver, J. M. Shull, S. A. Stern, P. Brandt, S. J. Conrad, G. R. Gladstone, C. M. Lisse, S. D. Porter, K. N. Singer, and A. J. Verbiscer, New Synoptic Observations of the Cosmic Optical Background with New Horizons, [arXiv e-prints](#), [arXiv:2407.06273 \(2024\)](#), [arXiv:2407.06273 \[astro-ph.GA\]](#).
- [47] A. Saldana-Lopez, A. Domínguez, P. G. Pérez-González, J. Finke, M. Ajello, J. R. Primack, V. S. Paliya, and A. Desai, An observational determination of the evolving extragalactic background light from the multiwavelength HST/CANDELS survey in the Fermi and CTA era, *Monthly Notices of the Royal Astronomical Society* **507**, 5144 (2021), [arXiv:2012.03035 \[astro-ph\]](#).
- [48] J. D. Finke, M. Ajello, A. Domínguez, A. Desai, D. H. Hartmann, V. S. Paliya, and A. Saldana-Lopez, *Modeling the Extragalactic Background Light and the Cosmic Star Formation History* (2022), [arXiv:2210.01157 \[astro-ph\]](#).
- [49] F. Haardt and P. Madau, Radiative Transfer in a Clumpy Universe. IV. New Synthesis Models of the Cosmic UV/X-Ray Background, *The Astrophysical Journal* **746**, 125 (2012), aDS Bibcode: 2012ApJ...746..125H.
- [50] K. Kawara, Y. Matsuoka, K. Sano, T. D. Brandt, H. Sameshima, K. Tsumura, S. Oyabu, and N. Ienaka, Ultraviolet to optical diffuse sky emission as seen by the hubble space telescope faint object spectrograph, *Publications of the Astronomical Society of Japan* **69**, 10.1093/pasj/psx003 (2017).
- [51] T. Matsumoto, M. G. Kim, J. Pyo, and K. Tsumura, *Re-analysis of near-infrared extragalactic background light based on the IRTS observation* (2015), [arXiv:1501.01359 \[astro-ph\]](#).
- [52] S. Matsuura, T. Arai, J. J. Bock, A. Cooray, P. M. Korngut, M. G. Kim, H. M. Lee, D. H. Lee, L. R. Levenson, T. Matsumoto, Y. Onishi, M. Shirahata, K. Tsumura, T. Wada, and M. Zemcov, New Spectral Evidence of an Unaccounted Component of the Near-infrared Extragalactic Background Light from the CIBER, *The Astrophysical Journal* **839**, 7 (2017), publisher: The American Astronomical Society.
- [53] N. Cappelluti, Y. Li, A. Ricarte, B. Agarwal, V. Alleavato, T. T. Ananna, M. Ajello, F. Civano, A. Comastri, M. Elvis, A. Finoguenov, R. Gilli, G. Hasinger, S. Marchesi, P. Natarajan, F. Pacucci, E. Treister, and C. M. Urry, The *Chandra* COSMOS Legacy Survey: Energy Spectrum of the Cosmic X-Ray Background and Constraints on Undetected Populations, *The Astrophysical Journal* **837**, 19 (2017).
- [54] M. Ajello, J. Greiner, G. Sato, D. R. Willis, G. Kanbach, A. W. Strong, R. Diehl, G. Hasinger, N. Gehrels, C. B. Markwardt, and J. Tueller, Cosmic X-Ray Background and Earth Albedo Spectra with *Swift* BAT, *The Astrophysical Journal* **689**, 666 (2008).
- [55] M. Revnivtsev, M. Gilfanov, R. Sunyaev, K. Jahoda, and C. Markwardt, The spectrum of the cosmic X-ray background observed by RXTE/PCA, *Astronomy and Astrophysics* **411**, 329 (2003), aDS Bibcode: 2003A&A...411..329R.
- [56] T. M. Kneiske, K. Mannheim, and D. H. Hartmann, Implications of Cosmological Gamma-Ray Absorption - I. Evolution of the Metagalactic Radiation Field, *Astronomy & Astrophysics* **386**, 1 (2002), [arXiv:astro-ph/0202104](#).
- [57] J. M. Overduin and P. S. Wesson, Dark Matter and Background Light, *Physics Reports* **402**, 267 (2004), [arXiv:astro-ph/0407207](#).
- [58] D. A. Forbes and T. J. Ponman, On the relationship between age and dynamics in elliptical galaxies, *Monthly Notices of the Royal Astronomical Society* **309**, 623 (1999), <https://academic.oup.com/mnras/article-pdf/309/3/623/2965674/309-3-623.pdf>.
- [59] M. Veale, C.-P. Ma, J. E. Greene, J. Thomas, J. P. Blakeslee, J. L. Walsh, and J. Ito, The MASSIVE survey - VIII. Stellar velocity dispersion profiles and environmental dependence of early-type galaxies, *Monthly Notices of the Royal Astronomical Society* **473**, 5446 (2017), <https://academic.oup.com/mnras/article-pdf/473/4/5446/22031016/stx2717.pdf>.
- [60] Y. Gong, A. Cooray, K. Mitchell-Wynne, X. Chen, M. Zemcov, and J. Smidt, Axion decay and anisotropy of near-IR extragalactic background light, *Astrophys. J.* **825**, 104 (2016), [arXiv:1511.01577 \[astro-ph.CO\]](#).
- [61] A. Charbonnier, C. Combet, and D. Maurin, CLUMPY: A code for γ -ray signals from dark matter structures, *Computer Physics Communications* **183**, 656 (2012), aDS Bibcode: 2012CoPhC.183..656C.
- [62] V. Bonnard, M. Hütten, E. Nezri, A. Charbonnier, C. Combet, and D. Maurin, CLUMPY: Jeans analysis, γ -ray and ν fluxes from dark matter (sub-)structures, *Computer Physics Communications* **200**, 336 (2016), aDS Bibcode: 2016CoPhC.200..336B.
- [63] M. Hütten, C. Combet, and D. Maurin, CLUMPY v3: γ -ray and ν signals from dark matter at all scales, *Computer Physics Communications* **235**, 336 (2019), aDS Bibcode: 2019CoPhC.235..336H.
- [64] J. F. Navarro, C. S. Frenk, and S. D. M. White, The Structure of Cold Dark Matter Halos, *ApJ* **462**, 563 (1996), [arXiv:astro-ph/9508025 \[astro-ph\]](#).

- [65] P. F. de Salas and A. Widmark, Dark matter local density determination: recent observations and future prospects, *Reports on Progress in Physics* **84**, 104901 (2021), [arXiv:2012.11477 \[astro-ph.GA\]](#).
- [66] A. Domínguez, J. R. Primack, D. J. Rosario, F. Prada, R. C. Gilmore, S. M. Faber, D. C. Koo, R. S. Somerville, M. A. Pérez-Torres, P. Pérez-González, J. S. Huang, M. Davis, P. Guhathakurta, P. Barmby, C. J. Conselice, M. Lozano, J. A. Newman, and M. C. Cooper, Extragalactic background light inferred from AEGIS galaxy-SED-type fractions, *MNRAS* **410**, 2556 (2011), [arXiv:1007.1459 \[astro-ph.CO\]](#).
- [67] Y.-T. Cheng, T. Arai, P. Bangale, J. J. Bock, T.-C. Chang, A. Cooray, R. M. Feder, P. M. Korngut, D. H. Lee, L. Liu, T. Matsumoto, S. Matsuura, C. H. Nguyen, K. Sano, K. Tsumura, and M. Zemcov, Probing Intra-Halo Light with Galaxy Stacking in CIBER Images, *The Astrophysical Journal* **919**, 69 (2021), aDS Bibcode: 2021ApJ...919...69C.
- [68] K. Mitchell-Wynne, A. Cooray, Y. Gong, M. Ashby, T. Dolch, H. Ferguson, S. Finkelstein, N. Grogin, D. Kocevski, A. Koekemoer, J. Primack, and J. Smidt, Ultraviolet luminosity density of the universe during the epoch of reionization, *Nature Communications* **6**, 7945 (2015), number: 1 Publisher: Nature Publishing Group.
- [69] C. Leitherer, D. Schaerer, J. D. Goldader, R. M. G. Delgado, C. Robert, D. F. Kune, D. F. de Mello, D. Devost, and T. M. Heckman, Starburst99: Synthesis Models for Galaxies with Active Star Formation, *The Astrophysical Journal Supplement Series* **123**, 3 (1999), aDS Bibcode: 1999ApJS..123...3L.
- [70] C. Leitherer, S. Ekström, G. Meynet, D. Schaerer, K. B. Agienko, and E. M. Levesque, The Effects of Stellar Rotation. II. A Comprehensive Set of Starburst99 Models, *The Astrophysical Journal Supplement Series* **212**, 14 (2014), aDS Bibcode: 2014ApJS..212...14L.
- [71] P. Kroupa, The Initial Mass Function of Stars: Evidence for Uniformity in Variable Systems, *Science* **295**, 82 (2002), [arXiv:astro-ph/0201098 \[astro-ph\]](#).
- [72] A. Tanikawa, T. Yoshida, T. Kinugawa, A. A. Trani, T. Hosokawa, H. Susa, and K. Omukai, Merger Rate Density of Binary Black Holes through Isolated Population I, II, III and Extremely Metal-poor Binary Star Evolution, *ApJ* **926**, 83 (2022), [arXiv:2110.10846 \[astro-ph.HE\]](#).
- [73] Fermi-LAT Collaboration, S. Abdollahi, M. Ackermann, *et al.*, A gamma-ray determination of the Universe's star formation history, *Science* **362**, 1031 (2018), [arXiv:1812.01031 \[astro-ph.HE\]](#).
- [74] C. Péroux and J. C. Howk, The Cosmic Baryon and Metal Cycles, *ARA&A* **58**, 363 (2020), [arXiv:2011.01935 \[astro-ph.GA\]](#).
- [75] H. A. Weaver, A. F. Cheng, F. Morgan, H. W. Taylor, S. J. Conard, J. I. Nunez, D. J. Rodgers, T. R. Lauer, W. M. Owen, J. R. Spencer, O. Barnouin, A. S. Rivkin, C. B. Olkin, S. A. Stern, L. A. Young, M. B. Tapley, and M. Vincent, In-flight performance and calibration of the long range reconnaissance imager (lorri) for the new horizons mission, *Publications of the Astronomical Society of the Pacific* **132**, pp. 1 (2020).
- [76] J. Koornneef, R. Bohlin, R. Buser, K. Horne, and D. Turnshek, Synthetic photometry and the calibration of the Hubble Space Telescope., *Highlights of Astronomy* **7**, 833 (1986).
- [77] K. Tsumura, T. Matsumoto, S. Matsuura, I. Sakon, and T. Wada, Low-Resolution Spectrum of the Extragalactic Background Light with the AKARI InfraRed Camera, *PASJ* **65**, 121 (2013), [arXiv:1307.6740 \[astro-ph.CO\]](#).
- [78] K. Mattila, K. Lehtinen, P. Väisänen, G. von Appen-Schnur, and C. Leinert, Spectrophotometric measurement of the Extragalactic Background Light, in *The Spectral Energy Distribution of Galaxies - SED 2011*, Vol. 284, edited by R. J. Tuffs and C. C. Popescu (2012) pp. 429–436, [arXiv:1111.6747 \[astro-ph.CO\]](#).
- [79] C. O'Hare, [cajohare/axionlimits: Axionlimits](#), <https://cajohare.github.io/AxionLimits/> (2020).
- [80] M. J. Dolan, F. J. Hiskens, and R. R. Volkas, Advancing globular cluster constraints on the axion-photon coupling, *J. Cosmology Astropart. Phys.* **2022**, 096 (2022), [arXiv:2207.03102 \[hep-ph\]](#).
- [81] K. Nakayama and W. Yin, Anisotropic cosmic optical background bound for decaying dark matter in light of the LORRI anomaly, *Physical Review D* **106**, 103505 (2022), [arXiv:2205.01079 \[astro-ph, physics:hep-ex, physics:hep-ph\]](#).
- [82] N. Cappelluti, G. Hasinger, and P. Natarajan, Exploring the High-redshift PBH- Λ CDM Universe: Early Black Hole Seeding, the First Stars and Cosmic Radiation Backgrounds, *ApJ* **926**, 205 (2022), [arXiv:2109.08701 \[astro-ph.CO\]](#).
- [83] M. Raue, T. Kneiske, and D. Mazin, First stars and the extragalactic background light: how recent γ -ray observations constrain the early universe, *A&A* **498**, 25 (2009), [arXiv:0806.2574 \[astro-ph\]](#).
- [84] A. Maurer, M. Raue, T. Kneiske, D. Horns, D. Elsässer, and P. H. Hauschildt, Dark Matter Powered Stars: Constraints from the Extragalactic Background Light, *ApJ* **745**, 166 (2012), [arXiv:1201.1305 \[astro-ph.CO\]](#).
- [85] P. Madau and M. Dickinson, Cosmic Star Formation History, *Annual Review of Astronomy and Astrophysics* **52**, 415 (2014), [arXiv:1403.0007 \[astro-ph\]](#).
- [86] P. Madau and T. Fragos, Radiation Backgrounds at Cosmic Dawn: X-Rays from Compact Binaries, *The Astrophysical Journal* **840**, 39 (2017), [arXiv:1606.07887 \[astro-ph\]](#).
- [87] M. Asplund, N. Grevesse, A. J. Sauval, and P. Scott, The Chemical Composition of the Sun, *ARA&A* **47**, 481 (2009), [arXiv:0909.0948 \[astro-ph.SR\]](#).
- [88] H. Dembinski and P. O. et al., [scikit-hep/iminuit 10.5281/zenodo.3949207](#) (2020).
- [89] M. Floc and B. Rocca-Volmerange, PÉGASE.3: A code for modeling the UV-to-IR/submm spectral and chemical evolution of galaxies with dust, *Astronomy & Astrophysics* **623**, A143 (2019).
- [90] S. G. Murray, B. Diemer, Z. Chen, A. G. Neuhold, M. A. Schnapp, T. Peruzzi, D. Blevins, and T. Engelman, THEHALOMOD: An online calculator for the halo model, *Astronomy and Computing* **36**, 100487 (2021), [arXiv:2009.14066 \[astro-ph.CO\]](#).
- [91] Götberg, Y., de Mink, S. E., Groh, J. H., Leitherer, C., and Norman, C., The impact of stars stripped in binaries on the integrated spectra of stellar populations, *A&A* **629**, A134 (2019).

Appendix A: Derivation of cosmic axion decay from first principles

The emissivity of axion decay is given by [57]

$$\varepsilon_{\lambda,a}(\lambda) = L_h \delta \left(\lambda - hc \frac{m_a c^2}{2} \right), \quad (\text{A1})$$

from which we see

$$\varepsilon_{\nu,a}(\lambda) = L_h \frac{\lambda^2}{c} \delta \left(\lambda - hc \frac{m_a c^2}{2} \right). \quad (\text{A2})$$

Inserting this into Eq. (1), we obtain

$$\nu I_\nu(\lambda, z) = \frac{c\lambda}{4\pi} L_h (1+z)^2 \int_{z_0}^{z_{\max}} \frac{dz'}{(1+z')^3 H(z')} \delta \left(\lambda \frac{1+z}{1+z'} - \frac{2hc}{m_a c^2} \right). \quad (\text{A3})$$

Changing variables of the integration from z' to $y = \lambda \frac{1+z}{1+z'} - \frac{2hc}{m_a c^2}$, we define z_* so that $y(z_*) = 0$. Now we can easily perform the integral and find

$$\nu I_\nu(\lambda, z) = \frac{c}{4\pi} L_h \frac{\Theta(z_* - z)}{H(z_*)} \frac{hc}{\lambda} \frac{2}{m_a c^2}. \quad (\text{A4})$$

Using the definition of L_h given by Eq. (6), we obtain Eq. (8).

Appendix B: COB model

Here, we provide details of the COB modeling.² First, we describe the complementary observational data and the theoretical background of the model. This leads to the fitting procedure and results. We also discuss how different model assumptions affect our results, as well as the impact additional subdominant components such as intrahalo light and stripped stars.

1. Emissivities, star formation rate, and metallicity evolution

For our COB model, we make use of additional observational data, which we describe in this subsection.

First, the galaxy emissivities have been obtained in the COB region. These measurements come from observations of resolved galaxies, detailing how much light these galaxies emit per wavelength and redshift. A compilation of emissivity values can be found in Finke22, and are plotted in Fig. 7.

Data of the star formation rate ρ_* as a function of redshift has been compiled in Ref. [73]. It is defined as the quantity of stars that form at any epoch per volume. There are different methods to measure ρ_* , such as luminosity measurements of galaxies in the ultraviolet and infrared, or using the nebular line emission that characterizes star formation [85]. They are plotted in Fig. 8.

Finally, we use measurements of the mean metallicity of the Universe as a function of redshift, in order to determine the metallicity of the stellar populations at any point in time. The observational data are taken from [74]. They are plotted in Fig. 9.

2. Details on the theoretical modeling of the COB

a. Stellar emissivities and synthetic spectra

A simple stellar population (SSP) is defined as a group of stars born from the same gas cloud, which then evolve with no further star formation [69]. The birth of the SSP lasts for megayears, so for cosmological purposes it can be assumed to be instantaneous. The stars in an SSP are assumed to share the same metallicity and age.

The emissivity of the stellar population can be calculated as

$$\varepsilon_{\nu,\text{stellar}}(\lambda, z) = f_{\text{esc,dust}} \times \int_z^{z_{\max}} L_\nu(t(z) - t(z')) \rho_*(z') \left| \frac{dt'}{dz'} \right| dz', \quad (\text{B1})$$

where L_ν is the luminosity of the SSP, ρ_* is the stellar formation rate, and $f_{\text{esc,dust}}$ is the fraction of light that escapes dust absorption. We integrate up to redshift $z_{\max} = 40$. The individual terms will be discussed below.

In order to study the behavior and evolution of stellar populations, it is necessary to turn to simulations. Several codes have been developed for this purpose and their output spectra $L_\nu(t)$ then serve as the input to calculate the stellar emissivities in Eq. (B1). In our case, STARBURST99 [69, 70] has been used to obtain the synthetic stellar spectra in our baseline model. We show them in Fig. 6.

We have used a Kroupa IMF, with $M_{\min} = 0.1 M_\odot$ and $M_{\max} = 120 M_\odot$ [71]. We follow the evolutionary Padova tracks.

b. The star formation rate ρ_*

The Star Formation Rate (SFR) ρ_* is the amount of SSPs that form at any epoch per unit volume. We follow Ref. [85] and parametrize the ρ_* as

$$\rho_*(z) = x_0 \frac{(1+z)^{x_1}}{1 + [(1+z)/x_2]^{x_3}}. \quad (\text{B2})$$

² The model is available online at https://github.com/axion-alp-dm/EBL_calculation

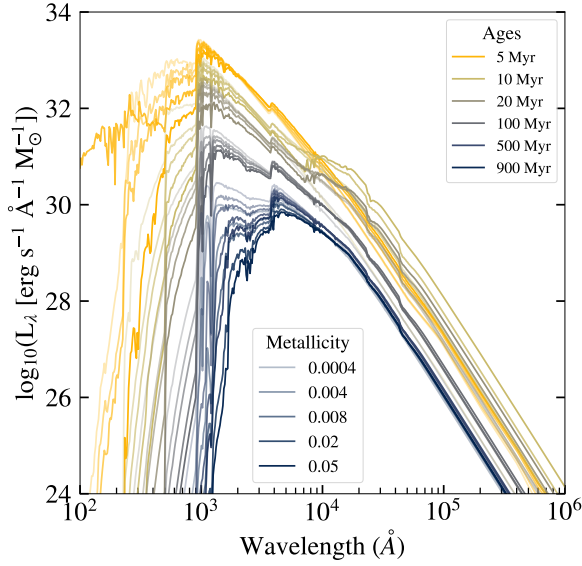


FIG. 6: SSP luminosities from the STARBURST99 code. Populations of different metallicities are shown with different line opacities, whereas the colors represent different ages.

The parameters x_i , $i = 1, 2, 3$ are determined by fitting it to the observations. The same approach has been used by, e.g., Refs. [48, 85, 86].

c. Dust escape fraction

The dust escape fraction $f_{\text{esc,dust}}$ is the fraction of photons that escape dust absorption. As we mentioned before, dust absorption plays an important role in the COB emission. The authors of Ref. [56] adopt an average fraction of photons that get absorbed at any point in time, disregarding the metallicity evolution. On the other hand, Finke22 implements a model relying on explicit redshift dependency, which we also follow here:

$$f_{\text{esc,dust}}(\lambda, z) = \frac{f_{\text{esc,dust}}(\lambda, z=0)}{f_{\text{esc,dust}}(\lambda = 0.15 \mu\text{m}, z=0)} 10^{-0.4A(z)}, \quad (\text{B3})$$

$$A(z) = m_d \frac{(1+z)^{n_d}}{1 + [(1+z)/p_d]^{q_d}}, \quad (\text{B4})$$

where $f_{\text{esc,dust}}$ is a stepwise function,

$$f_{\text{esc,dust}}(\lambda, z=0) = \begin{cases} f_{\text{esc},2} + (f_{\text{esc},2} - f_{\text{esc},1}) \cdot (\log_{10} \lambda - \log_{10} \lambda_2) / (\log_{10} \lambda_2 - \log_{10} \lambda_1) & \lambda \leq \lambda_2, \\ f_{\text{esc},3} + (f_{\text{esc},3} - f_{\text{esc},2}) \cdot (\log_{10} \lambda - \log_{10} \lambda_3) / (\log_{10} \lambda_3 - \log_{10} \lambda_2) & \lambda_2 < \lambda \leq \lambda_3, \\ f_{\text{esc},4} + (f_{\text{esc},4} - f_{\text{esc},3}) \cdot (\log_{10} \lambda - \log_{10} \lambda_4) / (\log_{10} \lambda_4 - \log_{10} \lambda_3) & \lambda_3 < \lambda \leq \lambda_4, \\ f_{\text{esc},5} + (f_{\text{esc},5} - f_{\text{esc},4}) \cdot (\log_{10} \lambda - \log_{10} \lambda_5) / (\log_{10} \lambda_5 - \log_{10} \lambda_4) & \lambda_4 < \lambda. \end{cases} \quad (\text{B5})$$

In Finke22, all λ_i , $i = 1, \dots, 5$ are fixed and the normalizations $f_{\text{esc,dust},i}$ and the parameters m_d , n_d , p_d , q_d are fitted to the data. Here, we use their best-fit parameters, $\lambda_i = (0.15, 0.167, 0.218, 0.422, 2.) \mu\text{m}$, $f_{\text{esc,dust},i} = (0.188, 0.218, 0.293, 0.393, 0.857)$, and $m_d = 1.49$, $n_d = 0.64$, $p_d = 3.4$, $q_d = 3.54$. We compare this characterization with the one given by Ref. [56],

$$f_{\text{esc,dust}} = 10^{-0.4A_\lambda}, \quad (\text{B6})$$

$$A_\lambda = 0.68 \cdot E(B-V) \cdot R \cdot (\lambda^{-1} - 0.35) \quad (\text{B7})$$

with $R = 3.2$, where A_λ is the absorption coefficient, and $E(B-V)$ is the color coefficient, which has to be measured and can depend on redshift [56]. Following Ref. [56] we neglect the redshift dependence and set $E(B-V) = 0.15$.

d. Mean metallicity evolution

The average metallicity is defined as the mean fraction of metals present in an epoch. We follow the parametrization from Ref. [72],

$$Z(z) = Z_\odot \times 10^{a_0 - a_1 \times z^{a_2}} \quad (\text{B8})$$

where Z_\odot is the solar metallicity, which we assume to be $Z_\odot = 0.02$ [87]. There is a degeneracy between the solar metallicity and a_0 , and we choose to fix Z_\odot and fit a_0 .

3. Fit to the data

In order to break the degeneracy between the axion and stellar components, we include additional data in

the COB model fit to constrain it. First, the stellar emissivity is constructed following Eq. (B1). The ρ_* follows the function in Eq. (B2), and the luminosities come from synthetic stellar spectra. The metallicity of the SSP follows the parametrization of Eq. (B8). As STARBURST99 SSPs are not available for metallicities $< 4 \times 10^{-4}$, we assume that the SSPs with lower metallicity share the same spectra as this limiting case. Using the emissivity, we can then calculate the CB spectrum following Eq. (1). This gives the CB spectrum of the stellar contribution.

We use the PYTHON package IMINUIT [88] in order to fit our model to the observational data, using the least squares method. The methodology is similar to the one used in Finke22. We free the ρ_* and Z parameters and fit our model to the compilations of ρ_* data, the emissivity data, the Z data and the COB galaxy counts that we described in Sec. II. Emissivities and COB galaxy counts have been calculated from direct galaxy measurements, so they can be used together to constrain the stellar population. This method gives information about the history of stellar formation. This leads to minimizing the following χ^2

$$\begin{aligned} \chi_{\text{COB}}^2 = & \sum_i \left(\frac{\nu I_{\nu, \text{model}}(\lambda_i) - \nu I_{\nu, i}}{\sigma_i} \right)^2 \\ & + \sum_i \left(\frac{\varepsilon_{\text{model}}(\lambda_i, z) - \varepsilon_i}{\sigma_i} \right)^2 \\ & + \sum_i \left(\frac{\rho_{*, \text{model}}(z_i) - \rho_{*, i}}{\sigma_i} \right)^2 \\ & + \sum_i \left(\frac{Z_{\text{model}}(z_i) - Z_i}{\sigma_i} \right)^2. \end{aligned} \quad (\text{B9})$$

The fits of our COB model to observational data are plotted in Fig. 7 for the emissivities, Fig. 8 for the ρ_* , Fig. 9 for Z and Fig. 1 and top panel of Fig. 2 for the COB intensity. Following Eq. (B9), we perform a combined fit of all these data with eight free parameters (the ρ_* and metallicity evolution parameters), which leaves 440 degrees of freedom. We impose no limits to the free parameters.

a. Results from the fit

The reduced χ^2 value for our model is $\chi_{\text{COB}}^2 = 2.7$. We show the best-fit parameters for our model in Table II. The fit is largely driven by the emissivity data, while the COB and Z data make up the smallest contributions to the χ^2 . Therefore, the inclusion of ρ_* and emissivity data completely fixes the COB.

At $\lambda \gtrsim 5 \mu\text{m}$ the dust reemission becomes the dominant component of the CB [37], so our fit takes into account CB data up to this wavelength. Our model fails to reproduce the upward trend after this point due to dust, which is visible in the Finke22 model in Fig. 1.

Parameter	Value
ρ_*	
x_0 ($M_{\odot}/\text{yr}/\text{Mpc}^3$)	$(1.302 \pm 0.032) \times 10^{-2}$
x_1	2.42 ± 0.04
x_2	3.317 ± 0.035
x_3	6.70 ± 0.07
Z	
a_0	-0.49 ± 0.04
a_1	0.022 ± 0.015
a_2	1.7 ± 0.4

TABLE II: Best-fit parameters for our model.

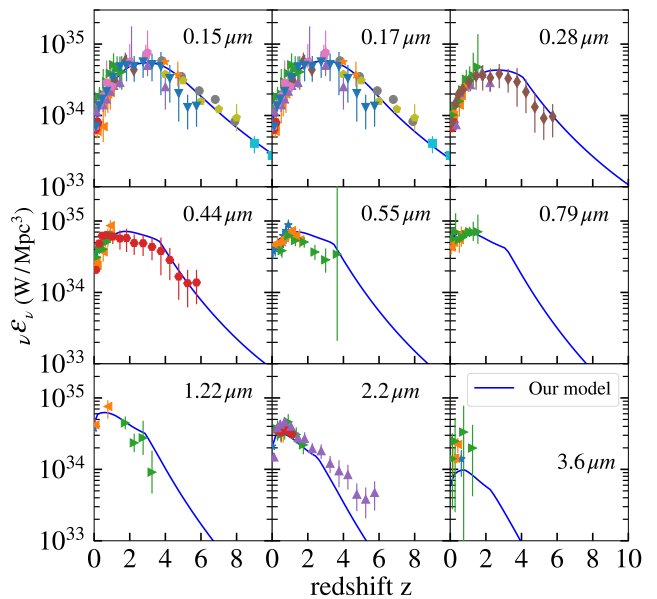


FIG. 7: Emissivity data for specific wavelengths as a function of redshift. Observational data is taken from the compilation by Finke22. Solid lines are our best-fit curves. The 1σ uncertainty band is too thin to be seen.

4. Systematic uncertainties

In order to assess the systematic uncertainties with respect to our model choices, we repeat our fits to the COB data with different assumptions. First, we used the code PÉGASE version 3.0.1 [89] to calculate stellar luminosities. These spectra are similar to those of STARBURST99, displaying differences especially at large wavelengths when the power-law regime settles at $\lambda \gtrsim 3 \times 10^4 \text{Å}$.

We also tried to use the Ref. [56] dust absorption, instead of the one in Finke22. This prescription ignores any redshift dependence, which affects the lower wavelength regime the most. There is a large amount of absorption at lower wavelengths, which results in higher emissions through the whole spectrum. This however, is at odds with the emissivity data.

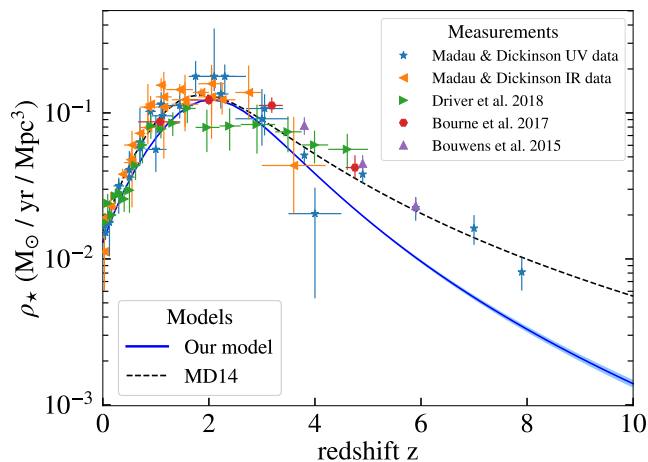


FIG. 8: The ρ_* as a function of redshift, with the 1σ uncertainty shown as a light blue band. Observational data compiled by [73] are shown with different symbols. The parametrization of Ref. [85] is shown as a dashed line for comparison.

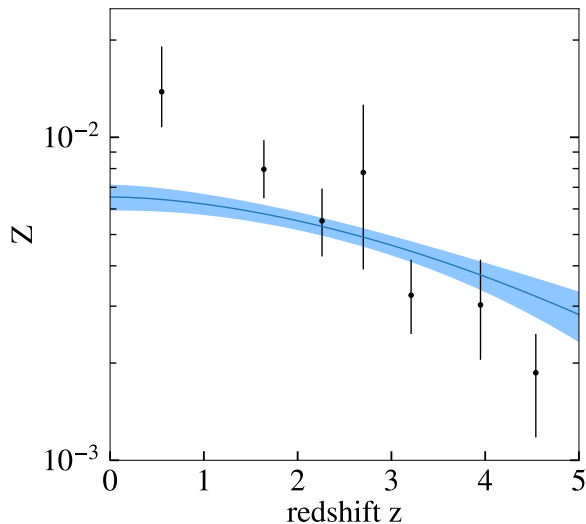


FIG. 9: The mean metallicity Z as a function of redshift. Observational data taken from Ref. [74]. Best-fit line and 1σ uncertainty are shown as a blue line and blue shaded region.

The results from the fits using these different model assumptions are summarized in Table III. We compare the results for all possible combinations of the considered dust absorption and SSP spectra. Our baseline model with STARBURST99 spectra and Finke22 dust absorption gives the overall best-fit result. Our model has the highest intensity in the LORRI band, and the biggest difference in mean intensity between models is of 14%, following Eq. (16).

Model	$\chi^2/\text{d.o.f.}$
Our model	$1169.2/440 = 2.7$
PÉGASE SSPs	$1571.5/440 = 3.6$
Kneiske dust absorption [56]	$2190.7/440 = 5.0$
PÉGASE SSPs and Kneiske dust absorption	$3818.7/440 = 8.7$

TABLE III: χ^2 values over degrees of freedom for the various model combinations described in the text.

5. Additional contributions

In addition to light from SSPs, the COB could also originate from other components. Here, we investigate some of them previously discussed in the literature and explain their contribution to our model.

a. Intrahalo light

The intrahalo light (IHL) is defined as the light created by stars that have been expelled from their host galaxy due to dynamical events. We follow the characterization described in Ref. [44], based on calculating the emissivity:

$$\varepsilon_{\lambda, \text{IHL}}(\lambda, z) = \int_{M_{\min}}^{M_{\max}} dM \frac{dn_{\text{h}}}{dM} L_{\lambda, \text{IHL}}(M, z), \quad (\text{B10})$$

where dn_{h}/dM is the halo mass function and $L_{\lambda, \text{IHL}}(M, z)$ is the IHL light specific luminosity emitted by a halo of mass M . We calculate the dn_{h}/dM with the HMF code [90], a specific tool for calculating halo mass functions. We use Ref. [44] to characterize $L_{\lambda, \text{IHL}}(M, z)$, taking their definition and reported mean values for the fraction of the total halo luminosity coming from IHL and redshift power-law dependence.

Without fitting the COB with the IHL, in Fig. 10 we show the IHL contribution summed to our model. The difference to our baseline model is negligible, only becoming relevant at large wavelengths. At $\lambda = 5\mu\text{m}$ (the maximum wavelength considered in our analysis), the IHL intensity is about 30% of the SSP intensity.

In the axion-photon parameter space, the IHL does lower the constraints of lighter axions. However, we have seen in the main text how differences between COB models affect the axion constraints in Fig. 2. Therefore, the impact of the IHL is negligible.

b. Stripped stars

Stars that strip their envelopes by interacting with a binary companion are defined as stripped. They emit a fraction of their radiation as ionizing photons, with energies larger than the usual stellar evolutionary tracks. Therefore, we test whether this extra component could also affect our models. We base our calculations on the

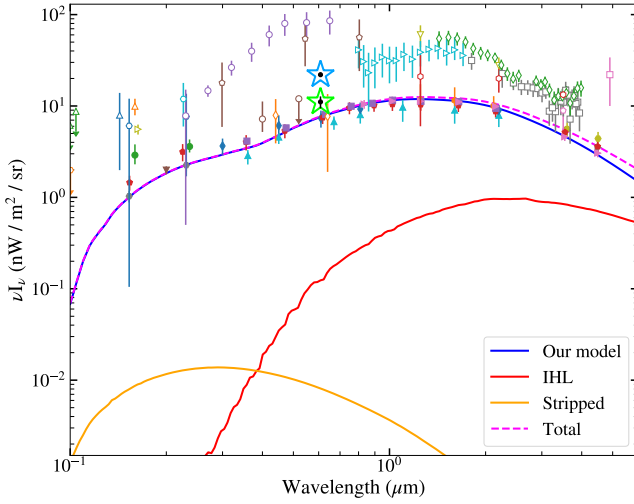


FIG. 10: Additional sources of the COB added to our model.

work of Ref. [91]. They calculate stellar spectra for these stripped stars, which we include in the COB calculation. The COB component of this extra contribution is at best 1% of the COB SSP intensity, as shown in Fig. 10.

Appendix C: Power-law dependence of axion constraints at higher masses

Looking at Fig. 3, we see that there is an almost power-law-like dependence of the constraints on $g_{a\gamma}$ at high masses in each CB region. In this appendix, we derive a relation that approximately describes this behavior. In Eq. (8) we see that

$$\nu I_\nu(\lambda, z) \propto \frac{(m_a c^2)^2 g_{a\gamma}^2}{\lambda H(z_*)}. \quad (\text{C1})$$

For high masses corresponding to a decay wavelength shorter than the shortest wavelength where data are available, $\lambda_{\min}^{\text{CiB}}$ ($i = \text{O, U, X}$), the limits will be dominated by the tail of the axion decay line (due to cosmic expansion) and its contribution to $\nu I_\nu(\lambda_{\min}^{\text{CiB}})$. Considering only this data point, we can solve Eq. (C1) for $g_{a\gamma}$ and use the definition of z_* from Eq. (9) to arrive at

$$g_{a\gamma} \propto \frac{[H(z_*)]^{1/2}}{m_a} = \frac{\sqrt{H_0} \left[\Omega_\Lambda + \Omega_m \left(\frac{m_a c^2}{2hc/\lambda_{\min}^{\text{CiB}}} \right)^3 \right]^{1/4}}{m_a}. \quad (\text{C2})$$

Thus, in the limit $m_a c^2 \gg hc/\lambda_{\min}^{\text{CiB}}$,

$$g_{a\gamma} \propto m_a^{-1/4}. \quad (\text{C3})$$

Fitting the slopes of our constraints numerically we find very good agreement with this approximation:

$$\begin{aligned} m_{\text{COB}} &= -0.2452 \pm 0.0003 \\ m_{\text{CUB}} &= -0.2339 \pm 0.0008 \\ m_{\text{CXB}} &= -0.2533 \pm 0.0004, \end{aligned}$$

with $g_{a\gamma} \propto (m_a c^2)^{m_{\text{CiB}}}$.